Materials Horizons

Over 31% Efficient Indoor Organic Photovoltaics Enabled by Simultaneously Reduced Trap-assisted Recombination and Non-radiative Recombination Voltage Loss

Journal:	*Materials Horizons*
Manuscript ID	MH-COM-10-2022-001229.R2
Article Type:	Communication
Date Submitted by the Author:	11-Nov-2022
Complete List of Authors:	Ma, Wei; Xi'an Jiaotong University, State Key Laboratory for Mechanical Behavior of Materials Zhou, Xiaobo; Xi'an Jiaotong University Wu, Hongbo; Donghua University Bothra, Urvashi; Indian Institute of Technology Bombay, c. Department of Physics Chen, Xingze; Chinese Academy of Sciences Suzhou Institute of Nano-tech and Nano-Bionics Lu, Guanyu; Xi'an Jiaotong University, Frontier Institute of Science and Technology Zhao, Heng; Xi'an Jiaotong University, State Key Laboratory for Mechanical Behavior of Materials Zhao, Chao; Xi'an Jiaotong University Luo, Qun; Suzhou Institute of Nano-tech and Nano-Bionics Chinese Academy of Sciences Lu, Guanghao; Xi'an Jiaotong University, Frontier Institute of Science and Technology; Xi'an Jiaotong University, b. School of Chemistry, Xi'an Jiaotong University, Xi'an 710049, China Zhou, Ke; Xi'an Jiaotong University, State Key Laboratory for Mechanical Behavior of Materials Kabra, Dinesh; Indian Institute of Technology Bombay, Physics Ma, Zaifei; Donghua University, Center for Advanced Low-dimension Materials

New concepts

Indoor organic photovoltaics (OPVs) have been considered as a major breakthrough in the application of self-sustainable indoor electronic devices. Previous studies have shown that the layer-by-layer (LBL) film with ideal interface contacts is conductive to reduce the trap-assisted recombination, thereby improve the fill factor (FF) and power conversion efficiency (PCE) of indoor OPVs. However, the significant contribution of V_{OC} for efficient indoor devices is currently ingored because the relationship between voltage losses and LBL morphology still remains obscure. Herein, after finely optimizing the bulk and interface morphology of PM6:Y6-O system during LBL processing, the optimal LBL device obtained a record PCE of 31.2% under 1000 lux light-emitting diode among indoor OPVs mainly due to its excellent FF (81.5%) and reduced voltage losses. Detailed characterizations revealed that the stronger crystallinity, purer domain and ideal interfacial contacts in LBL devices can simultaneously reduce the trap-assisted recombination, leakage current and non-radiative recombination voltage loss, compared to their bulk-heterojunction counterparts. Besides, this work demonstrated that the LBL strategy had great potential in promoting the commercialization of indoor OPVs, as it can promote the device performance universally confirmed in other efficient systems and increase the long-term stability of indoor OPVs.

ARTICLE

Over 31% Efficient Indoor Organic Photovoltaics Enabled by Simultaneously Reduced Trap-assisted Recombination and Non-radiative Recombination Voltage Loss

Received 00th January 20xx,
Accepted 00th January 20xx

DOI: 10.1039/x0xx00000x

Xiaobo Zhou,[a] Hongbo Wu,[b] Urvashi Bothra,[c] Xingze Chen,[d] Guanyu Lu,[e] Heng Zhao,[a] Chao Zhao,[a] Qun Luo,[d] Guanghao Lu,[e] Ke Zhou,*[a] Dinesh Kabra,*[c] Zaifei Ma*[b] and Wei Ma*[a]

Indoor organic photovoltaics (OPVs) have shown great potential application in driving low energy consumption electronics of Internet of Things. There is still great room for further improving the power conversion efficiency (PCE) of indoor OPVs, considering that the desired morphology of the active layer to reduce the trap-assisted recombination and voltage losses, and thus simultaneously enhance the fill factor (FF) and open-circuit voltage for efficient indoor OPVs still remains obscure. Herein, by optimizing the bulk and interface morphology via layer-by-layer (LBL) processing strategy the low leakage current and low non-radiative recombination loss can be synergistically achieved in PM6:Y6-O based devices. Detailed characterizations reveal the stronger crystallinity, purer domain and ideal interfacial contacts in LBL devices, compared to their bulk-heterojunction (BHJ) counterparts. The optimized morphology yields a reduced voltage loss and an impressive FF of 81.5%, and thus contributes to a high PCE of 31.2% under 1000 lux light-emitting diode (LED) in LBL devices, which is the best reported efficiency for indoor OPVs. Besides, this LBL strategy exhibits great universality in promoting the performance of indoor OPVs, as exemplified by three other non-fullerene acceptor systems. This work provides the guidelines for morphology optimization and synergistically promotes the fast development of efficiently indoor OPVs.

Introduction

Due to the rapid development of non-fullerene acceptor and its derivatives, the power conversion efficiencies (PCEs) of single-junction organic photovoltaics (OPVs) have exceeded 19% under AM 1.5G illumination (1 sun).[1-3] The continuously improved device performance provides the opportunities to focus on promoting the application of OPVs. Recently, OPVs have exhibited the favourable potential to persistently power the nodes for wireless technologies and large networks of connected devices by harvesting ambient light, which makes indoor OPVs attract great attention.[4-9] Compared to inorganic materials, organic materials used as the active layer of indoor OPVs possess strong absorbance in the visible light region (390–760 nm), which matches better with the spectra of indoor light sources such as light-emitting diodes (LED) and fluorescent light (FL).[10] Therefore, the theoretic PCE of indoor OPVs is more than 50%, which is much higher than that under 1 sun.[11] Although there is a large amount of works prompting the performance of indoor OPVs and the best PCE is around 30%,[10, 12-15] there is still great room for further improving the performance of indoor OPVs.

Apart from the variation of spectrum, the charge carrier density of indoor OPVs is typically 2-3 orders lower, when changing illumination conditions from 1 sun to indoor light.[16] Therefore, there are two essential demands for an ideal indoor OPV. Firstly, to obtain a high short-circuit current density (J_{SC}), the absorption of active layer should be tuned to well match the indoor light spectrum and the external quantum efficiency (EQE) in the visible range should be as high as possible. Secondly, the charge recombination and voltage losses should be simultaneously reduced to achieve a high fill factor (FF) and open-circuit voltage (V_{OC}). Due to the low charge carrier density of indoor light sources, the influence of bimolecular recombination is ignorable

[a] State Key Laboratory for Mechanical Behavior of Materials, Xi'an Jiaotong University, Xi'an 710049, China. E-mail: msewma@xjtu.edu.cn; msekzhou@xjtu.edu.cn.
[b] Advanced Low-dimension Materials, State Key Laboratory for Modification of Chemical Fibers and Polymer Materials, Center for College of Materials Science and Engineering, Donghua University, Shanghai 201620, China. E-mail: mazaifei@dhu.edu.cn.
[c] Department of Physics, Indian Institute of Technology, Mumbai, 400076 India. E-mail: dkabra@phy.iitb.ac.in.
[d] i-Lab & Printable Electronics Research Center, Suzhou Institute of Nano-Tech and Nano-Bionics, Chinese Academy of Sciences, Suzhou, 215123 China
[e] Frontier Institue of Science and Technology, Xi'an Jiaotong University, Xi'an 710054, China.
Electronic Supplementary Information (ESI) available: [details of any supplementary information available should be included here]. See DOI: 10.1039/x0xx00000x

for indoor OPVs. However, the leakage current and trap-assisted recombination which are usually negligible under 1 sun will have a dramatic effect on indoor OPVs performance.[13, 17-20] Here, the magnitude of the leakage current is determined by the value of shunt resistance (R_{sh}). The higher R_{sh}, the less current that goes through the device.[20] According to the equivalent circuit model, at low light intensities, the effects of shunt resistance on FF can be expressed based on the following equation:[17]

$$FF \approx FF_0[1 - \frac{(v_{oc} + 0.7)V_{OC}FF_0}{v_{oc} * I_{SC} \quad R_{sh}}] \quad (1)$$

where the $FF_0 = \frac{v_{oc} - \ln(v_{oc} + 0.72)}{v_{oc} + 1}$, and $v_{oc} = \frac{eV_{OC}}{nkT}$, respectively. As depicted in above equation, the FF will dramatically decrease as the R_{sh} decreases under low light intensities. On the other hand, according to the relationship $V_{OC} \propto \log(P_{in})$, where P_{in} is the incident light intensity, there is an extra V_{OC} loss above 0.1 V for a common OPV device, when varying the light intensity from AM 1.5G to indoor light (1000 lux LED).[21] This V_{OC} loss can be effectively reduced by suppressing the trap-assisted recombination. In addition, the voltage loss induced by non-radiative recombination should also be inhibited in order to obtain a high V_{OC}. In short, when the absorption of active layer well covers the visible light, the leakage current, trap-assisted recombination and non-radiative recombination voltage loss should be significantly reduced so as to achieve both high FF and V_{OC} for efficient indoor OPVs.

Currently, the bulk-heterojunction (BHJ) active layers are usually employed in most of the indoor OPVs.[22-27] Recently, Ko et al.[28] chose a highly crystalline acceptor (ITIC-Th) which had comparable solubility with the acceptor IT-4F and incorporated it with the non-fullerene blend (PM6:IT-4F). The ITIC-Th can act as a morphology controller in the ternary blend to improve the molecular packing and arrangement of PM6 as well as IT-4F. Therefore, the optimized morphological properties including the phase separation and crystallinity facilitate a high PCE of 30.11% for ternary device under 500 lux LED. However, the non-ideal interface due to the physical contact between donor and electron transport layer (ETL) or between acceptor and hole transport layer (HTL) will induce charge recombination and hinder charge collection.[29-31] The increased recombination, especially the trap-assisted recombination will cause more dramatic drops of V_{OC} and FF,[13, 18, 20] indicating that the BHJ morphology is intrinsically not the best choice for indoor OPVs. On the other hand, under 1 sun conditions, some works have demonstrated that the layer-by-layer (LBL) strategy by sequential deposition is an effective method to induce the formation of vertical phase distribution with acceptor enriched at the ETL and donor enriched at the HTL. Such ideal interface contact can suppress the trap-assisted recombination losses and promote charge transport.[29-34] For example, Kim et al.[18] used LBL strategy to manufacture the indoor OPVs and found obvious PCE enhancement under 1000 lux for LBL device due to increased FF. Compared to BHJ structures, the LBL film exhibited more favorable mrophology with ideal interface contacts. However, the significant contribution of V_{OC} for efficient indoor devices is currently ingored because the relationship between voltage losses and LBL morphology still remains obscure. Therefore, the typical features of bulk and interface morphology which will be in favor of simultaneously decreasing the trap-assisted recombination and non-radiative recombination voltage loss, and consequently facilitating the FF and V_{OC} for the efficient indoor OPVs need to be further investigated.

In this work, the LBL indoor photovoltaic devices based on PM6 and Y6-O were fabricated via sequential processing, and the morphology-dependent device performance under indoor light (LED) was investigated in detail. After finely adjusting the morphology, the optimal LBL device obtained a record PCE of 31.2% under 1000 lux LED among indoor OPVs mainly due to its excellent FF (81.5%) and better V_{OC}, which are much higher than that of the corresponding BHJ devices. The LBL film can form the desired vertical phase distribution with PM6-enrichment at bottom in conventional devices, and the stronger crystallinity and higher domain purity can be concomitantly observed. This favourable morphology facilitates the charge transport, and reduces the trap-assisted recombination, leakage current and energy loss, which simultaneously promote the FF and V_{OC} of indoor OPVs. Moreover, the LBL strategy can effectively increase the long-term stability of indoor OPVs due to the optimized phase separation. This work highlights the relationship between morphology and devices performance, and demonstrates excellent universality of the LBL strategy in enhancing photovoltaic performances of indoor OPVs.

Results and discussion

The PM6:Y6-O BHJ device has been reported for its high efficiency under indoor light.[13] In this work, the conventional device structure with the geometry of ITO/PEDOT:PSS/active layer/PDINO/Al based on PM6:Y6-O was also utilized to fabricate LBL devices. The details of device fabrication can be found in Supporting Information. **Figure 1a** shows the chemical structures of PM6 and Y6-O. The PM6 shows an absorption peak at 614 nm and a shoulder at 576 nm, while the Y6-O possesses an absorption peak at 776 nm (**Figure S1a**). Both the absorption spectra of BHJ and LBL films (300-800 nm) match the LED spectra well, as shown in **Figure S1b**. The absorption peak of acceptor in the LBL film exhibits a slight red-shift (from 764 nm to 768 nm), indicating its more aggregated Y6-O compared to the BHJ film. The *J-V* curves of BHJ and LBL devices under 1 sun illumination are presented in **Figure 1b** and their photovoltaic parameters are summarized in **Table 1**. The LBL device presents a slightly higher J_{SC} (22.8 mA/cm^2) than that of BHJ device (22.5 mA/cm^2). As shown in **Figure S1c**, the LBL device shows higher EQE values at the wavelength ranging from 600 to 800 nm than that of BHJ device. Therefore, the corresponding integrated current density (J_{EQE}) of LBL device calculated from EQE spectra is higher than that of BHJ

device, and the J_{EQE}s are consistent with their J_{SC} values. Besides, the LBL device exhibits a higher V_{OC} of 0.975 V and FF of 77.5% compared to those of BHJ device (V_{OC}, 0.957 V; FF, 76.0%). Eventually, a better PCE of 17.2% is achieved for the LBL device.

To explain their performance differences, especially on J_{SC} and FF differences, we investigated exciton dissociation and recombination dynamics. As shown in **Figure S2a**, we applied the photoluminescence (PL) analysis of BHJ and LBL films to evaluate the exciton dissociation behaviours,[35, 36] where the excitation wavelength of 740 nm was used. The exciton quenching efficiency is represented by PL quenching rate in **Table S1**. The PL quenching rate of LBL film (99.0%) is higher than that of BHJ films (98.2%), indicating its slightly higher dissociation efficiency. The photocurrent density (J_{ph}) was analyzed as a function of effective applied voltage (V_{eff}) to investigate the charge extraction of the devices,[37] as shown in **Figure S2b**. The exciton dissociation probability (P_{diss}) is calculated by $P_{diss} = J_{ph}/J_{sat}$ at short-circuit condition and the results are shown in **Table S1**. Both the devices can reach saturated current when the V_{eff} is high, indicating the effective charge carriers collection. The higher P_{diss} (96.8%) of LBL device confirms its more efficient exciton dissociation. These results are consistent with their J_{SC}. To study the charge transport properties, the electron mobility (μ_e) and hole mobility (μ_h) were measured by space-charge-limited current (SCLC) method. As shown in **Figure S3** and **Table S2**, the LBL device shows a higher μ_e of 1.24×10^{-4} $cm^2V^{-1}s^{-1}$ and thus a more balanced hole and electron mobility (μ_h/μ_e = 1.02), compared to the BHJ device (μ_e = 1.07×10^{-4} $cm^2V^{-1}s^{-1}$; μ_h/μ_e = 1.15). Balanced mobility will reduce charge accumulation and suppress the charge recombination, thereby facilitate a higher FF of LBL devices.[38] The dependences of V_{OC} and J_{SC} on the light intensity at logarithmic forms were analyzed to investigate the charge recombination mechanism.[39, 40] If the Shockley-Read-Hall (SRH) recombination is involved, a strong dependence of V_{OC} on light intensity with a slope larger than 1 kT/q will be observed. As shown in **Figure S4a**, the slope of LBL device (1.01 kT/q) is smaller than that of BHJ device (1.05 kT/q), representing its lower trap-assisted recombination, which possibly induces dramatic difference in their performance under indoor light illuminance. Furthermore, the fitted slopes (α) of J_{SC} vs light intensity curves are 0.972 and 0.995 for the BHJ and LBL devices, respectively (**Figure S4b**). The larger α of LBL device reveals its lower bimolecular recombination, which contributes to its higher FF.

Considering the high V_{OC} and EQE values in the range of visible light, the photovoltaic performances of corresponding devices under the indoor light conditions were investigated. The light intensities of 250, 500 and 1000 lux are selected to meet the illuminance demand of indoor applications. The light power intensities of LED (3000 K) were measured and calculated as the reported paper.[12] The *J-V* curves of BHL and LBL devices are presented in **Figure 1c** and **Figure S5**, and their corresponding parameters are summarized in **Table 2**. It is clear that the LBL devices can achieve better performance than BHJ devices under all light intensities. The LBL device shows an excellent PCE of 31.2% (V_{OC}, 0.866 V; J_{SC}, 134.9 μA/cm^2; FF, 81.5%) under 1000 lux. Notably, this FF and PCE are the best values among indoor OPVs to the best of our knowledge, as shown in **Figure 1d and Table S3**. Even when the light intensity was decreased to 500 and 250 lux, the LBL device can achieve impressive PCEs of 30.3% and 29.2%, respectively. As shown in **Figure S6a**, the integrated current density J_{cal}s are calculated to be 128.6, 64.3 and 32.2 μA/cm^2 under 1000, 500 and 250 lux, respectively, which only have small deviations (<5%) from the J_{SC} values obtained based on *J-V* curves. The BHJ device exhibits a lower PCE of 28.8% (V_{OC}, 0.840 V; J_{SC}, 133.8 μA/cm^2; FF, 78.4%) under 1000 lux compared to LBL device. Beside, when the light intensity is reduced to 500 and 250 lux, the BHJ device only exhibits lower PCEs of 27.5% and 25.3%, respectively. The J_{cal}s of BHJ device are calculated to be 127.6, 63.8 and 31.9 μA/cm^2 under 1000, 500 and 250 lux (**Figure S6b**), respectively, which are also consistent with the J_{SC} values obtained from *J-V* curves. Noteworthy, the indoor BHJ devices show higher FF and V_{OC}, but lower J_{SC} and PCE compared to that of the literature[13] under LED illumination, which may be due to the differences of LED spectrum and calibration.

The light intensity-dependent performance of BHJ and LBL devices under LED illumination is further analyzed to investigate the charge recombination under low carrier densities. The *J-V* curves and corresponding parameters of BHL and LBL devices under 125 and 1500 lux are presented in **Figure S7** and **Table S4**. The dependence of V_{oc} on light intensity curves are shown in **Figure S8a**. The fitted slopes of BHJ and LBL devices are 1.39 kT/q and 1.23 kT/q, respectively, which are clearly higher than those under outdoor lighting conditions, indicating severe effect of trap-assisted recombination on indoor OPVs performance. Meanwhile, the smaller slope of LBL device indicates its lower trap-assisted recombination than that of BHJ device. The LBL device can maintain high FFs (> 80%) in a wide range of light intensity (250 to 1500 lux), as shown in **Figure 1e**. However, the FFs of BHJ device significantly decrease with the decrement of light intensity. The slopes α of J_{SC} vs light intensity curves are much close to 1, which confirms that bimolecular recombination is both negligible for BHJ and LBL devices under low light intensity (**Figure S8b**). Eventually, the small variations of V_{OC} and FF lead to the smaller PCE decrement of LBL device as the decrease of light intensity than that of BHJ device, as shown in **Figure 1f**. The LBL device maintains a high PCE of 26.6% even under 125 lux, which is much higher than that of BHJ device (21.8%).

Grazing incidence wide angle X-ray scattering (GIWAXS)[41, 42], resonant soft X-ray scattering (RSoXS)[43] and atomic force microscope (AFM) were employed to investigate the correlation between active layer morphology and device performance. The 2D GIWAXS diffraction patterns and the corresponding line profiles of pure PM6, Y6-O, their BHJ and LBL films are illustrated in **Figure S9** and **Figure 2a**. It is shown that the PM6 and Y6-O

exhibit the pronounced (010) diffraction peaks at q_z =1.70 Å^{-1} and 1.81 Å^{-1}, respectively, in the out-of-plane direction, indicating the preferential face-on orientation of molecule ordering in both neat films. Similar peak positions at around q_z =1.80 Å^{-1} are recorded for the BHJ and LBL films, indicating that this peak mainly belongs to the (010) diffraction peak of Y6-O. The fitting results of (010) peaks of corresponding films are summarized in **Table S5**. The LBL films exhibit a higher coherence length (CL) of π-π stacking (27.8 Å), compared to BHJ film (CL of 27.3 Å), indicating its stronger crystallinity of Y6-O. The enhanced Y6-O crystallinity probably contributes to the charge transport, thus a higher μ_e of LBL device. Then the film surface morphology was revealed by AFM measurements. As shown in **Figure 2b**, both BHJ and LBL films exhibit low root-mean-square (RMS) roughness values of 1.02 and 0.97 nm, respectively, indicating that the surface roughness is not the major cause for their different device performance. The extent of phase separation in films was measured by RSoXS. The domain size and domain purity can be extracted from fitting the scattering profiles, as shown in **Figure 2c** and **Table S5**. The BHJ and LBL films present the domain sizes of 20.7 and 22.5 nm, respectively. The bigger domain size in LBL film may be attributed to the strong crystallinity induced the phase separation. Besides, the LBL film exhibits a higher relative domain purity compared to that of BHJ film, which could effectively supress the charge recombination.

LBL processing is an appropriate method designed to control the vertical phase distribution. Therefore, we adopted a facile approach of film-depth-dependent light absorption spectra to further investigate the variations of donor and acceptor composition in the vertical direction.[44, 45] The film-depth-dependent light absorption spectra of the BHJ and LBL films are illustrated in **Figure S10a** and **Figure S10b**, and the extracted sub-layer absorption spectra are shown in **Figure S10c** and **Figure S10d**. The stronger donor PM6 absorption than acceptor Y6-O at the bottom indicates that there are more PM6-rich regions at the bottom of BHJ and LBL films. Combined with the neat film absorption spectra of PM6 and Y6-O, the component ratio and calculated D/A ratio can be obtained as depicted in **Figure S10e, Figure S10f** and **Figure 2d**. The approximately homogeneous distributions of PM6 and Y6-O from the top surface to the depth around 85 nm are found in both BHJ and LBL films. However, compared to BHJ film, the LBL film exhibits significantly higher D/A ratio at the bottom, indicating that there are more donor PM6 accumulated at the bottom. The time of flight secondary ion mass spectrometry (TOF-SIMS) was further utilized to monitor their difference in the vertical phase distribution.[34] Of note is that cyanogroup (CN^-) was used to track the acceptor Y6-O. After analyzing the CN^- signal and CN^- intensity ratio (CN^-(BHJ)/CN^-(LBL)) as depicted in **Figure 2e** and **Figure 2f**, it can be concluded that the polymer donor PM6 is enriched at the bottom and Y6-O acceptor gathers at the top few nanometers in LBL film. The favourable vertical phase separation can effectively reduce the trap-assisted recombination and suppress the leakage current at the interface of active layer/ETL (HTL). The middle part of LBL film possesses similar donor and acceptor vertical distributions with BHJ film, indicating the BHJ-like morphology at the middle part of LBL film. The well-mixed middle part provides sufficient D/A interfaces for charge separation, together with the better charge transport, thus the LBL device can obtain a slightly larger J_{SC} than that of BHJ device. Therefore, combining all the results from these morphology characterizations, the detailed vertical phase separation in optimized BHJ and LBL films can be depicted, as presented in the inset of **Figure 2d**. The distinct difference in vertical texture of BHJ and LBL films is directly reflected in their device properties, especially at low light intensities.

The device physical properties involving leakage current, traps and charge recombination losses are investigated in detail to further understand the intrinsic mechanism of the morphology induced performance enhancement. Firstly, we measured the dark *J–V* curves to check the difference in leakage current, where the dark current is usually dominated by the leakage current at low bias voltage. As shown in **Figure 3a**, it is apparent that the LBL device presents around one order of magnitude lower dark current and thus a much higher shunt resistance than those of BHJ device (**Table 1**). This is one of the key reasons why the LBL indoor device obtains significantly higher FF than that of BHJ indoor device. We speculated that the strong crystallinity, large and pure domains (less boundaries for leakage)[46] and ideal interface contact all contribute to the low leakage current of LBL device. To distinguish the leakage current of bulk phase and interface is beyond the scope of this work. For LBL devices with the same film thickness, it is demonstrated that the leakage current will decrease as the donor thickness increases (probably more donor enriched at the bottom), indicating the LBL sequential processing is an effective strategy to control the leakage current, as shown in **Figure 3b**. The optimized LBL device with 50 nm (PM6) and 60 nm (Y6-O) presents the low leakage current and best performance, as shown in **Figure S11 and Table S6**.

The SCLC measurements are further utilized to analysis the trap density of BHJ and LBL devices.[47] For the hole- and electron-only devices, a part of the injected current will be captured by the traps, which causes an abrupt transition from the space charge limited regime to the trap filled limit. This process is evident in the *J-V* curves as an abrupt increase of the current at a voltage called trap-filled limit voltage (V_{TFL}), as shown in **Figure S12a**. The trap density (N_t) can be estimated by the equation:

$$N_t = \frac{2\varepsilon_r\varepsilon_0}{eL^2}V_{TFL} \quad (2)$$

Where L is film thickness, ε_r is permittivity of the semiconductor, ε_0 is the permittivity of free space. The LBL device shows a lower V_{TFL}, thus its electron trap density (N_t ~ 1.5×10^{22} m^{-3}) is lower than that of BHJ device (N_t ~ 1.7×10^{22} m^{-3}). The transient photocurrent (TPC) measurements can provide the information on carrier

transport and, in particular, on whether traps affect the transport in devices.[48] As shown in **Figure S12b** and **Figure 3c**, the current signal of LBL device is slightly larger than that of BHJ device, which is consistent with the trend of their J_{SC}. Besides, the transport time of LBL device (0.69 μs) is significantly faster than that of BHJ device (1.27 μs), suggesting its less trapping and thus more efficient charge transport. Additionally, the charge carrier lifetimes of BHJ and LBL devices were investigated by the transient photovoltage (TPV) measurements.[49] As shown in **Figure S13**, the LBL device exhibits obviously larger charge carrier lifetimes, which may be ascribed to its less charge recombination, compared to BHJ device.[50, 51] These results can be sufficient to account for the difference of their FFs under 1 sun and indoor light illumination.

Voltage loss measurements were carried out to determine the recombination losses in BHJ and LBL systems. The voltage loss can be further divided to find the contribution from each component based on the Shockley–Queisser (SQ) model[52].

$$\Delta V_{OC} = \left(\frac{E_g}{q} - V_{OC}^{SQ}\right) + \left(V_{OC}^{SQ} - V_{OC}^{SC}\right) + \left(V_{OC}^{SC} - V_{OC}^{rad}\right) + (V_{OC}^{rad} - V_{OC}) \quad (3)$$

$$\Delta V_{OC} = \Delta V_{OC}^{SQ} + \Delta V_{gen} + \Delta V_{rad}^{band-tail} + \Delta V_{non-rad} \quad (4)$$

where q is the elementary charge, E_g is the bandgap, which is defined from the derivative of the EQE edge (**Figure S14a**). V_{OC}^{SQ} is the thermodynamic limit of the V_{OC} at a given optical band gap, V_{OC}^{SC} is the current limited SQ limit of V_{OC} due to the non-unity EQE of devices above the bandgap, and V_{OC}^{rad} is the radiative limit of V_{OC} where the radiative recombination is assumed to be the sole recombination channel in the device. The V_{OC}^{SC} and V_{OC}^{rad} are calculated from the high-sensitive EQE (EQE_{sen}) spectra corrected by electroluminescence (EL) spectra (**Figure S14b**), AM 1.5 solar photon flux density, and blackbody photon flux density[52, 53]. The $\Delta V_{non\text{-}rad}$ is determined by the EQE_{EL} of the OPVs: $\Delta V_{non-rad} = \frac{kT}{q} ln\left(\frac{1}{EQE_{EL}}\right)$. As shown in **Figure 3d**, the LBL device exhibits a higher EQE_{EL} value (8.91×10^{-5}) than that of BHJ device (5.91×10^{-5}). Therefore, the LBL device possesses a lower non-radiative recombination loss of 0.232 eV, compared to that of BHJ device (0.244 eV). Although the E_g of LBL device is smaller than that of BHJ device, the non-radiative recombination loss of LBL device is lower, resulting in its lower E_{loss} and higher V_{OC}. The results obtained from the calculation is shown in **Table 3** and depicted in **Figure 3e**. In addition, when the light intensity decreases from 1 sun to 1000 lux LED, the LBL device will suffer a smaller extra V_{OC} loss due to its supressed trap-assisted recombination, compared to the BHJ device. Therefore, the LBL device obtains much higher V_{OC} under indoor light intensity.

The different processing conditions of active layer additionally affects the interfacial energetics; therefore, we also analyzed the D:A interface and charge transfer (CT) binding energy in these device.[54] The energy of CT state (E_{CT}) is calculated using high-sensitive EQE measurements by fitting the CT spectral region of EQE with the below equation[55]:

$$EQE_{sen} \propto \frac{1}{\sqrt{4\pi\lambda kT}} \exp\left(\frac{-(E_{CT} + \lambda - E)^2}{4\lambda kT}\right) \quad (5)$$

where λ is reorganization energy, k is Boltzmann constant, T is absolute temperature and E is the photon energy. **Figure 3f** shows the EQE spectrum for both the devices fitted using equation 5. The extracted interfacial parameters λ and E_{CT} are shown in **Table 3.**

The reorganization energy is correlated with the interfacial disorder as it signifies the broadening of CT states. The reorganization energy increases from 70 to 79 meV on changing the processing from LBL to BHJ, indicating higher energetic disorder at the D:A interface for BHJ in contrast to the LBL devices. The higher disorder at the CT interface results in larger non-radiative recombination in the devices, therefore, reducing the V_{OC} for BHJ devices.[56] We also measured the degree of energetic disorder in the bulk by calculating Urbach energy (E_U) using the below expression[57]:

$$EQE(E) \propto \exp\left(\frac{E}{E_U}\right) \quad (6)$$

The bulk E_U calculated is ~ 23 meV for both the devices. To understand the energetic disorder in both the devices without the contribution from CT state disorder, we subtracted the CT state absorption from the total absorption and the result is shown in **Figure S15**[52]. The E_U calculated from EQE w/o CT state contribution is ~22 meV, indicating similar bulk disorder in both the devices. Interestingly, these results suggest that the different active layer processing predominantly affects the D:A interface, which results in disordered interface and higher voltage losses for BHJ devices. Therefore, LBL processing is a preferred technique to reduce the CT state disorder and the voltage losses. These findings suggest that BHJ puts a steric hinderance and/or vibrational coupling in reduction of interfacial disorder.[58, 59]

Based on all the above results, the correlation between the morphology of the active layer and the performances of indoor OPVs could be analyzed in a more systematic way. Compared to the BHJ film, the LBL film possesses stronger crystallinity, bigger domain size and better phase separation, which is better for the charge transport. Besides, the LBL film exhibits a higher relative domain purity, which could effectively supress the charge recombination. The polymer donor PM6 is enriched at the bottom and Y6-O acceptor gathers at the top few nanometers in LBL film. This favourable vertical phase distribution induces more ideal interface contact, which could also facilitate the charge transport. We speculate that the strong crystallinity, large and pure domains and ideal interface contact all contribute to the low trap-assisted recombination and leakage current, which promote the FF and decrease the extra V_{OC} loss (due to the decreasing of light intensity) of LBL indoor OPVs. Furthermore, all the favourable morphology features of the LBL film contribute to the reduced CT state disorder and non-radiative recombination loss,

and thus decreased voltage losses. Therefore, the LBL indoor OPVs can simultaneously achieve much higher FF and V_{OC}, compared to those of the BHJ indoor OPVs.

We also investigated the storage stability for LBL and BHJ devices in the nitrogen atmosphere with the temperature of ≈25 ℃. As shown in **Figure 4a**, under 1000 lux LED illumination, unencapsulated LBL devices exhibit superior stability and maintain ≈98% of the original PCE after storage for 500 hours, compared to ≈93% of the BHJ devices. The excellent stability of LBL devices under weak light illumination suggests the great potential in practical indoor applications. Under 1 sun illumination, both the BHJ and LBL devices suffer a faster decrease of PCEs, as shown in **Figure 4b**. However, the LBL devices still exhibit better stability over a long time, which can maintain above 86% of the original PCE after storage for 500 hours, compared to the ≈ 80% of the BHJ devices. The morphology degradation has been proved to be responsible for the performance degradation of OPVs.[28] We believe that the LBL processing strategy promotes more favourable phase separation and purer phases, which is in a more stable thermodynamic state, and thus guarantees the superior long-term stability of OPVs.[60] To further verify the universality of such sequential processing strategy, three different devices based on PM6:BTA3, PM6:Y6 and PCE10:$PC_{70}BM$ systems were fabricated with the same device structure. The experiment results demonstrate that the PCEs of both LBL devices are higher than those of BHJ devices under 1 sun, as shown in **Figure S16** and **Table S7**. Besides, all the LBL devices show lower dark current than corresponding BHJ devices (**Figure S17**). Eventually, the PM6:BTA3, PM6:Y6 and PCE10:$PC_{70}BM$ LBL devices all exhibit much higher PCE under 1000 lux LED, which is mainly attributed to the significant improvement of V_{OC} and FF, as shown in **Figure 4c**, **Figure 4d, Figure S18** and **Table S8**.

Conclusions

In conclusion, the performance of indoor OPVs has been successfully improved due to the morphology manipulation via LBL processing strategy. It is demonstrated that the LBL film exhibits stronger crystallinity, purer domain and optimized vertical phase distribution with ideal interface contacts, which is conducive to the charge transport, and reducing the recombination loss and leakage current. All those favorable photoelectric processes simultaneously promote the FF and V_{OC}, thus contribute to an impressive PCE of indoor LBL OPVs, where the FF of 81.5% and PCE of 31.2% are the highest values of indoor OPVs reported so far. Besides, the experiment results validated that the LBL strategy can improve the performance of indoor OPVs universally and increase the device stability under 1 sun and indoor light. This work provides the guidelines for morphology optimization by revealing the structure-performance correlation and synergistically promotes the fast development of efficiently indoor OPVs.

Author contribution statement

Xiaobo Zhou fabricated the solar cell devices and performed the UV-vis, PL, and AFM measurements; Hongbo Wu performed the energy loss and TPC tests; Urvashi Bothra helped interpret the energy loss data; Guanyu Lu performed the film-depth-dependent light absorption spectra measurements; Xingze Chen performed the TOF-SIMS measurements; Heng Zhao and Baojun Lin helped analyze the data; Dinesh Kabra proposed constructive opinions for the energy loss analysis; Zaifei Ma helped analysed the energy loss and TPC data; Wei Ma and Ke Zhou conceived and directed the experiment. All authors contributed to analysis and manuscript writing.

Conflicts of interest

There are no conflicts to declare.

Acknowledgements

Thanks for the support from NSFC (52173023, 21875182, 52073056), Key Scientific and Technological Innovation Team Project of Shaanxi Province (2020TD-002), 111 project 2.0 (BP2018008). X-ray data was acquired at beamlines 7.3.3 and 11.0.1.2 at the Advanced Light Source, which is supported by the Director, Office of Science, Office of Basic Energy Sciences, of the U.S. Department of Energy under Contract No. DE-AC02-05CH11231. The authors thank Dr. Eric Schaible and Dr. Chenhui Zhu at beamline 7.3.3, and Dr. Cheng Wang at beamline 11.0.1.2 for assistance with data acquisition.

References

1. L. Zhu, M. Zhang, J. Xu, C. Li, J. Yan, G. Zhou, W. Zhong, T. Hao, J. Song, X. Xue, Z. Zhou, R. Zeng, H. Zhu, C. C. Chen, R. C. I. MacKenzie, Y. Zou, J. Nelson, Y. Zhang, Y. Sun, F. Liu, *Nat. Mater.*, 2022, **21**, 656.
2. Y. Wei, Z. Chen, G. Lu, N. Yu, C. Li, J. Gao, X. Gu, X. Hao, G. Lu, Z. Tang, J. Zhang, Z. Wei, X. Zhang, H. Huang, *Adv. Mater.*, 2022, **34**, e2204718.
3. C. He, Y. Pan, Y. Ouyang, Q. Shen, Y. Gao, K. Yan, J. Fang, Y. Chen, C.-Q. Ma, J. Min, C. Zhang, L. Zuo, H. Chen, *Energy Environ. Sci.*, 2022, **15**, 2537.
4. P. P. Ray, J. King Saud Univ. *Comput. Inf. Sci.*, 2018, **30**, 291.
5. I. Mathews, S. N. Kantareddy, T. Buonassisi, I. M. Peters, *Joule*, 2019, **3**, 1415.
6. A. Al-Fuqaha, M. Guizani, M. Mohammadi, M. Aledhari, M. Ayyash, *IEEE Commun. Surv. Tutor.*, 2015, **17**, 2347.

7. J. Gubbi, R. Buyya, S. Marusic, M. Palaniswami, *Futur. Gener. Comp. Syst.*, 2013, **29**, 1645.
8. J. A. Khan, H. K. Qureshi, A. Iqbal, *Comput. Electr. Eng.*, 2015, **41**, 159.
9. J. Russo, W. Ray, M. S. Litz, *Appl. Energy*, 2017, **191**, 10.
10. Y. Cui, H. Yao, T. Zhang, L. Hong, B. Gao, K. Xian, J. Qin, J. Hou, *Adv. Mater.*, 2019, **31**, 1904512.
11. J. K. W. Ho, H. Yin, S. K. So, *J. Mater. Chem. A*, 2020, **8**, 1717.
12. Y. Cui, Y. M. Wang, J. Bergqvist, H. F. Yao, Y. Xu, B. W. Gao, C. Y. Yang, S. Q. Zhang, O. Inganas, F. Gao, J. H. Hou, *Nat. Energy*, 2019, **4**, 768.
13. L.-K. Ma, Y. Chen, P. C. Y. Chow, G. Zhang, J. Huang, C. Ma, J. Zhang, H. Yin, A. M. Hong Cheung, K. S. Wong, S. K. So, H. Yan, *Joule*, 2020, **4**, 1486.
14. F. Bai, J. Zhang, A. Zeng, H. Zhao, K. Duan, H. Yu, K. Cheng, G. Chai, Y. Chen, J. Liang, W. Ma, H. Yan, *Joule*, 2021, **5**, 1231.
15. Z. Chen, T. Wang, Z. Wen, P. Lu, W. Qin, H. Yin, X.-T. Hao, *ACS Energy Lett.*, 2021, **6**, 3203.
16. R. Steim, T. Ameri, P. Schilinsky, C. Waldauf, G. Dennler, M. Scharber, C. J. Brabec, *Sol. Energy Mater. Sol. Cells*, 2011, **95**, 3256.
17. S. C. Shin, C. W. Koh, P. Vincent, J. S. Goo, J. H. Bae, J. J. Lee, C. Shin, H. Kim, H. Y. Woo, J. W. Shim, *Nano Energy*, 2019, **58**, 466.
18. S. Y. Park, C. Labanti, J. Luke, Y. C. Chin, J. S. Kim, *Adv. Energy Mater.*, 2021, **12**, 2103237.
19. Y. Zhou, T. M. Khan, J. W. Shim, A. Dindar, C. Fuentes-Hernandez, B. Kippelen, *J. Mater. Chem. A*, 2014, **2**, 3492.
20. C. M. Proctor, T.-Q. Nguyen, *Appl. Phys. Lett.*, 2015, **106**, 083301.
21. T. Zhang, C. An, Y. Cui, J. Zhang, P. Bi, C. Yang, S. Zhang, J. Hou, *Adv. Mater.*, 2022, **34**, e2105803.
22. H. K. H. Lee, J. Wu, J. Barbé, S. M. Jain, S. Wood, E. M. Speller, Z. Li, F. A. Castro, J. R. Durrant, W. C. Tsoi, *J. Mater. Chem. A*, 2018, **6**, 5618.
23. Y. J. You, C. E. Song, Q. V. Hoang, Y. Kang, J. S. Goo, D. H. Ko, J. J. Lee, W. S. Shin, J. W. Shim, *Adv. Funct. Mater.*, 2019, **29**, 1901171.
24. M. Nam, H. Y. Noh, J. Cho, Y. Park, S. C. Shin, J. A. Kim, J. Kim, H. H. Lee, J. W. Shim, D. H. Ko, *Adv. Funct. Mater.*, 2019, **29**, 1900154.
25. M. Nam, J. H. Kang, J. Shin, J. Na, Y. Park, J. Cho, B. Kim, H. H. Lee, R. Chang, D. H. Ko, *Adv. Energy Mater.*, 2019, **9**, 1901856.
26. S. Park, H. Ahn, J.-y. Kim, J. B. Park, J. Kim, S. H. Im, H. J. Son, *ACS Energy Lett.*, 2019, **5**, 170.
27. H. I. Je, E. Y. Shin, K. J. Lee, H. Ahn, S. Park, S. H. Im, Y. H. Kim, H. J. Son, S. K. Kwon, *ACS Appl. Mater. Interfaces*, 2020, **12**, 23181.
28. C. Lee, J. H. Lee, H. H. Lee, M. Nam, D. H. Ko, *Adv. Energy Mater.*, 2022, **12**, 2200275.
29. R. Sun, Q. Wu, J. Guo, T. Wang, Y. Wu, B. Qiu, Z. Luo, W. Yang, Z. Hu, J. Guo, M. Shi, C. Yang, F. Huang, Y. Li, J. Min, *Joule*, 2020, **4**, 407.
30. R. Sun, J. Guo, Q. Wu, Z. Zhang, W. Yang, J. Guo, M. Shi, Y. Zhang, S. Kahmann, L. Ye, X. Jiao, M. A. Loi, Q. Shen, H. Ade, W. Tang, C. J. Brabec, J. Min, *Energy Environ. Sci.*, 2019, **12**, 3118.
31. Q. Li, L.-M. Wang, S. Liu, L. Guo, S. Dong, G. Ma, Z. Cao, X. Zhan, X. Gu, T. Zhu, Y.-P. Cai, F. Huang, *ACS Energy Lett.*, 2020, **5**, 3637.
32. S. Dong, K. Zhang, B. Xie, J. Xiao, H.-L. Yip, H. Yan, F. Huang, Y. Cao, *Adv. Energy Mater.*, 2019, **9**, 1802832.
33. R. Sun, J. Guo, C. Sun, T. Wang, Z. Luo, Z. Zhang, X. Jiao, W. Tang, C. Yang, Y. Li, J. Min, *Energy Environ. Sci.*, 2019, **12**, 384.
34. L. Zhan, S. Li, X. Xia, Y. Li, X. Lu, L. Zuo, M. Shi, H. Chen, Adv. Mater. 2021, 33, 2007231.
35. L. Zhang, B. Lin, Z. Ke, J. Chen, W. Li, M. Zhang, W. Ma, *Nano Energy*, 2017, **41**, 609.
36. J. Fang, Z. Wang, J. Zhang, Y. Zhang, D. Deng, Z. Wang, K. Lu, W. Ma, Z. Wei, *Adv.Sci.*, 2015, **2**, 1500250.
37. M. Lenes, M. Morana, C. J. Brabec, P. W. M. Blom, *Adv. Funct. Mater.*, 2009, **19**, 1106.
38. L. Zhang, B. Lin, B. Hu, X. Xu, W. Ma, *Adv. Mater.*, 2018, **30**, 1800343.
39. L. J. A. Koster, V. D. Mihailetchi, H. Xie, P. W. M. Blom, *Appl. Phys. Lett.*, 2005, **87**, 203502.
40. L. J. A. Koster, V. D. Mihailetchi, R. Ramaker, P. W. M. Blom, *Appl. Phys. Lett.*, 2005, **86**, 123509.
41. A. Hexemer, W. Bras, J. Glossinger, E. Schaible, E. Gann, R. Kirian, A. MacDowell, M. Church, B. Rude, H. Padmore, *J. Phys.: Conf. Ser.*, 2010, **247**, 012007.
42. P. Muller-Buschbaum, *Adv. Mater.*, 2014, **26**, 7692.
43. E. Gann, A. T. Young, B. A. Collins, H. Yan, J. Nasiatka, H. A. Padmore, H. Ade, A. Hexemer, C. Wang, *Rev. Sci. Instrum.*, 2012, **83**, 045110.
44. Z. Wang, Y. Hu, T. Xiao, Y. Zhu, X. Chen, L. Bu, Y. Zhang, Z. Wei, B. B. Xu, G. Lu, *Adv. Opt. Mater.*, 2019, **7**, 1900152.
45. L. Bu, S. Gao, W. Wang, L. Zhou, S. Feng, X. Chen, D. Yu, S. Li, G. Lu, *Adv. Electron. Mater.*, 2016, **2**, 1600359.
46. X. Zhou, H. Wu, B. Lin, H. B. Naveed, J. Xin, Z. Bi, K. Zhou, Y. Ma, Z. Tang, C. Zhao, Q. Zheng, Z. Ma, W. Ma, *ACS Appl. Mater. Interfaces*, 2021, **13**, 44604.
47. D. Abbaszadeh, A. Kunz, G. A. Wetzelaer, J. J. Michels, N. I. Craciun, K. Koynov, I. Lieberwirth, P. W. Blom, *Nat. Mater.*, 2016, **15**, 628.
48. O. Alqahtani, M. Babics, J. Gorenflot, V. Savikhin, T. Ferron, A. H. Balawi, A. Paulke, Z. Kan, M. Pope, A. J. Clulow, J. Wolf, P. L. Burn, I. R. Gentle, D. Neher, M. F. Toney, F. Laquai, P. M. Beaujuge, B. A. Collins, *Adv. Energy Mater.*, 2018, **8**, 1702941.
49. W. M. M. Lin, D. Bozyigit, O. Yarema, V. Wood, *J. Phys. Chem. C*, 2016, **120**, 12900.
50. W. Huang, E. Gann, N. Chandrasekaran, L. Thomsen, S. K. K. Prasad, J. M. Hodgkiss, D. Kabra, Y.-B. Cheng, C. R. McNeill, *Energy Environ. Sci.*, 2017, **10**, 1843.

51. Z. Li, F. Gao, N. C. Greenham, C. R. McNeill, *Adv. Funct. Mater.*, 2011, **21**, 1419.
52. N. Jain, R. Sharma, S. Mahesh, D. Moghe, H. J. Snaith, S. Yoo, D. Kabra, *ACS Appl. Mater. Interfaces*, 2021, **13**, 60279.
53. J. Wang, X. Jiang, H. Wu, G. Feng, H. Wu, J. Li, Y. Yi, X. Feng, Z. Ma, W. Li, K. Vandewal, Z. Tang, *Nat. Commun.*, 2021, **12**, 6679.
54. H. Fu, Y. Wang, D. Meng, Z. Ma, Y. Li, F. Gao, Z. Wang, Y. Sun, *ACS Energy Lett.*, 2018, **3**, 2729.
55. K. Vandewal, K. Tvingstedt, A. Gadisa, O. Inganäs, J. V. Manca, *Physical Review B*, 2010, **81**, 125204.
56. N. Jain, N. Chandrasekaran, A. Sadhanala, R. H. Friend, C. R. McNeill, D. Kabra, *J. Mater. Chem. A*, 2017, **5**, 24749.
57. N. Jain, U. Bothra, D. Moghe, A. Sadhanala, R. H. Friend, C. R. McNeill, D. Kabra, *ACS Appl Mater Interfaces*, 2018, **10**, 44576.
58. K. R. Graham, C. Cabanetos, J. P. Jahnke, M. N. Idso, A. El Labban, G. O. Ngongang Ndjawa, T. Heumueller, K. Vandewal, A. Salleo, B. F. Chmelka, A. Amassian, P. M. Beaujuge, M. D. McGehee, *J. Am. Chem. Soc.*, 2014, **136**, 9608.
59. S. Illig, A. S. Eggeman, A. Troisi, L. Jiang, C. Warwick, M. Nikolka, G. Schweicher, S. G. Yeates, Y. Henri Geerts, J. E. Anthony, H. Sirringhaus, *Nat. Commun.*, 2016, **7**, 10736.
60. Y. Wang, Q. Zhu, H. B. Naveed, H. Zhao, K. Zhou, W. Ma, *Adv. Energy Mater.*, 2020, **10**, 1903609.

ARTICLE

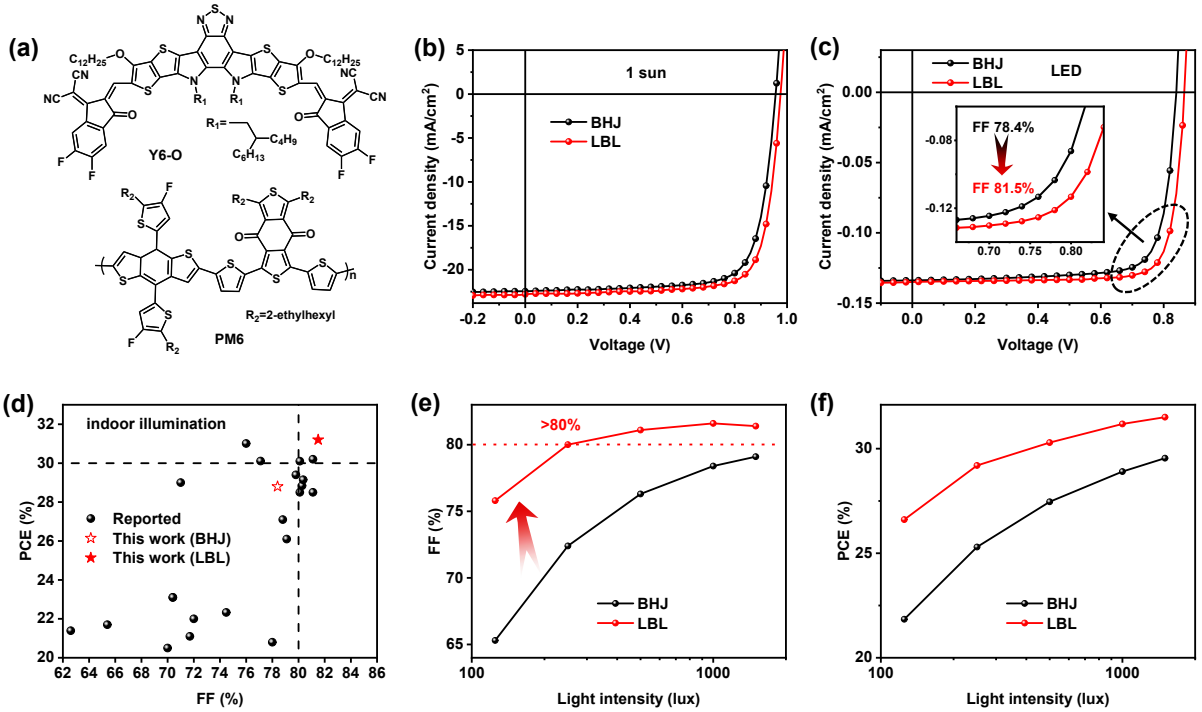

Fig. 1. (a) Chemical structures of PM6 and Y6-O; *J-V* curves of BHJ and LBL devices under (b) 1 sun and (c) 1000 lux LED illuminance, the inset is the *J-V* curves near the maximum power point; (d) the plots of PCE versus FF for efficiently indoor OPVs in the literature; dependence of (e) FF and (f) PCE on indoor light intensity of BHJ and LBL devices.

ARTICLE

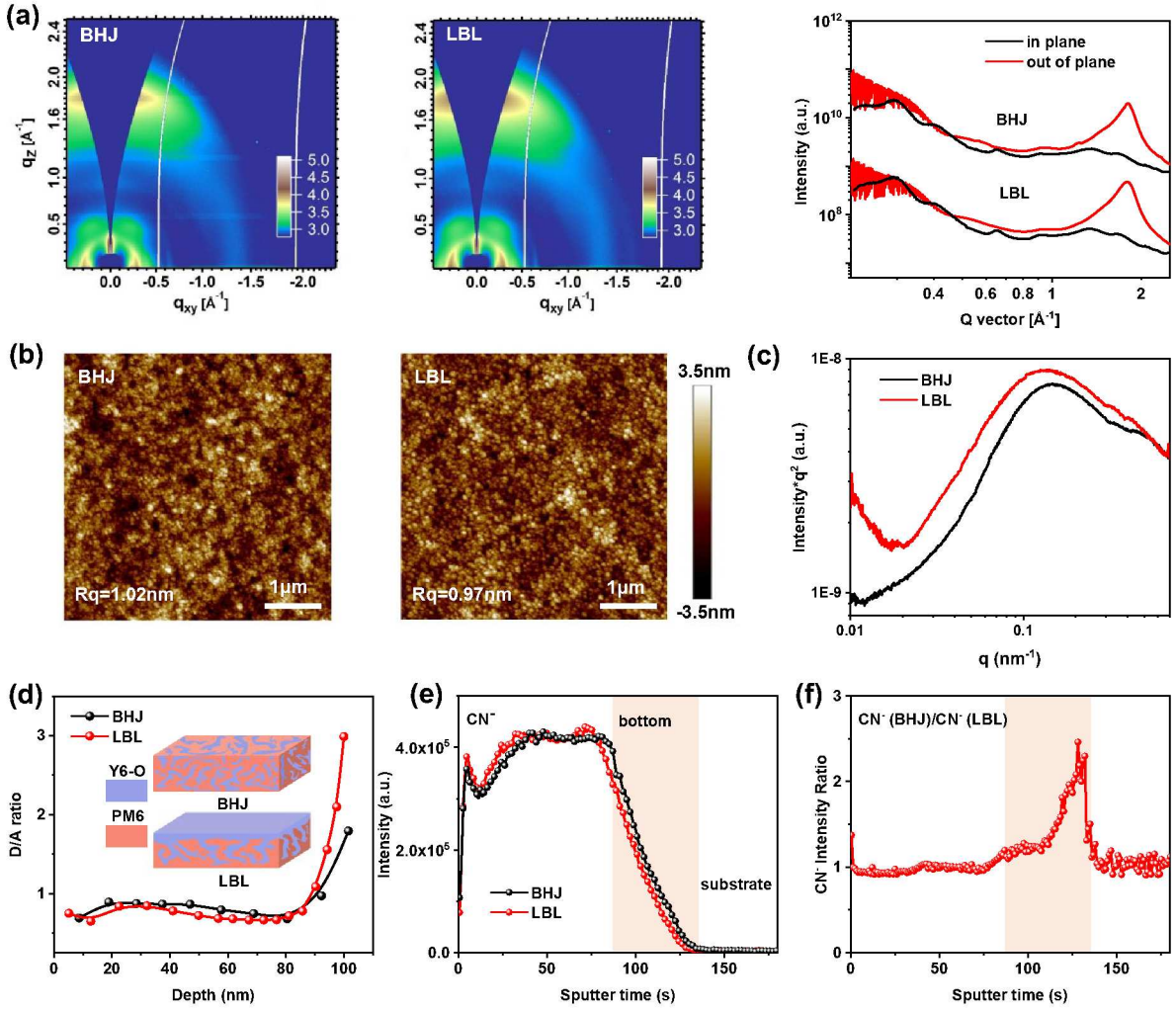

Fig. 2. (a) GIWAXS 2D profiles of BHJ and LBL films, and their GIWAXS line profiles; (b) AFM height images of BHJ and LBL films; (c) RSoXS profiles of corresponding films; (d) the calculated D/A ratio at the film-depth from the film-depth-dependent absorption spectra; TOF-SIMS ion yield of CN^- of (e) BHJ and LBL films; and (f) their CN^- intensity ratio as a function of sputtering time.

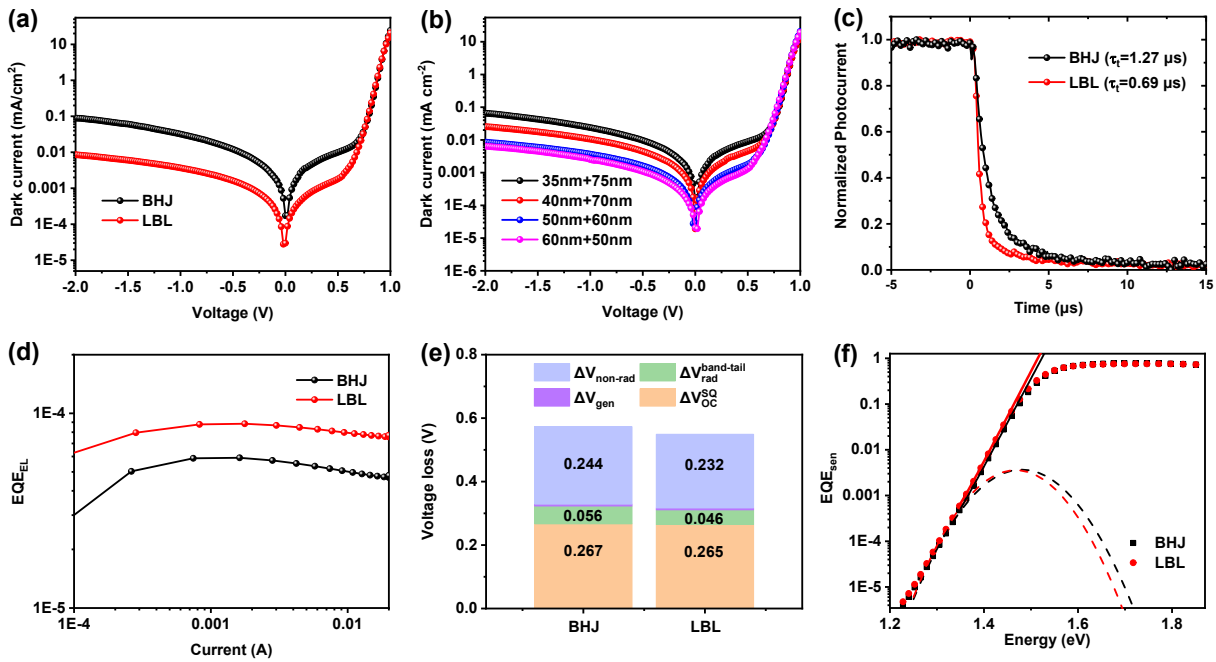

Figure 3. (a) The dark *J-V* curves of the optimized BHJ and LBL devices; (b) The dark *J-V* curves of LBL devices with different donor and acceptor thickness; (c) Photocurrent transients of BHJ and LBL devices; (d) EQE_{EL} and (e) energy loss for BHJ and LBL devices; (f) Sensitive EQE spectrum of PM6:Y6-O BHJ and LBL devices fitted with equation 5.

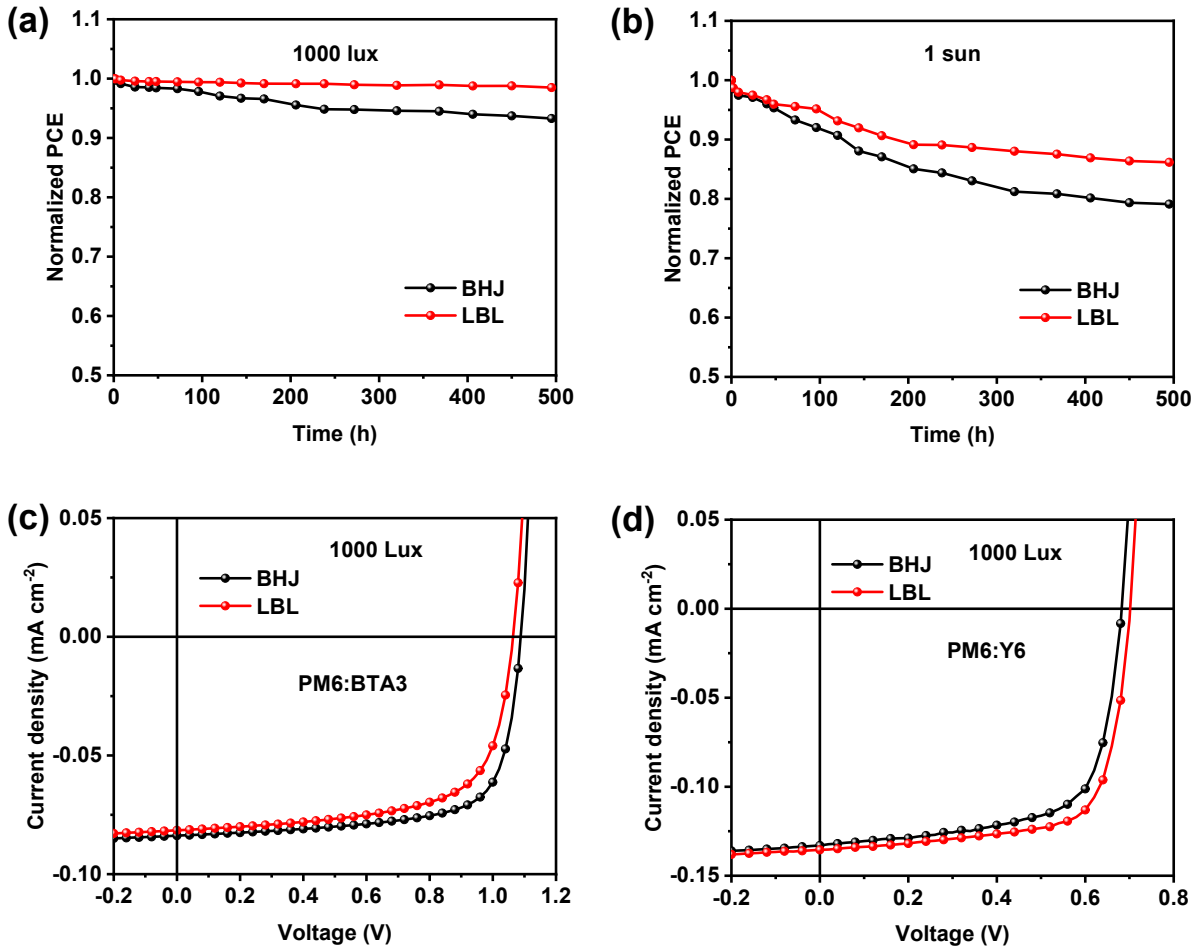

Figure 4. Normalized PCE of PM6:Y6-O based BHJ and LBL devices as a function of time in nitrogen atmosphere under (a) 1000 lux LED and (b) 1 sun intensity. The *J-V* curves of BHJ and LBL devices based on (c) PM6:BTA3 and (d) PM6:Y6 systems under 1000 lux LED.

Table 1. Photovoltaic parameters of the BHJ and LBL devices under 1 sun illumination.

Active layer	V_{OC} (V)	FF (%)	J_{SC} (mA/cm^2)	PCE (%)[a]	J_{EQE} (mA/cm^2)	R_{sh} (kΩ cm^2)	R_s (Ω cm^2)
BHJ	0.957	76.0	22.5	16.4 (15.9±0.2)	22.1	57.5	4.76
LBL	0.975	77.5	22.8	17.2 (16.8±0.5)	22.6	343	5.54

[a)] The average parameters were calculated from over 10 devices.

Table 2. Photovoltaic parameters of the BHJ and LBL devices under LED illumination.

Active layer	Light intensity (lux)	P_{in} (μW/cm^2)	V_{OC} (V)	J_{SC} (μA/cm^2)	J_{cal}[a] (μA/cm^2)	FF (%)	PCE (%)[b]
BHJ	1000	306.2	0.840	133.8	127.6	78.4	28.8 (28.1±0.5)
	500	153.1	0.820	66.9	63.8	76.3	27.5 (26.7±0.6)
	250	76.6	0.796	33.5	31.9	72.4	25.3 (24.6±0.3)
LBL	1000	306.2	0.866	134.9	128.6	81.5	31.2 (30.3±0.6)
	500	153.1	0.846	67.4	64.3	81.1	30.3 (29.6±0.8)
	250	76.6	0.825	33.7	32.2	80.0	29.2 (28.5±0.4)

[a)]The J_{cal} were calculated from EQE spectra;

[b)] The average parameters were calculated from over 10 devices.

Table3. Detailed E_{loss} of BHJ and LBL devices based on PM6:Y6-O system.

Active layer	E_g/q (V)	ΔV_{OC}^{SQ} (V)	$\Delta V_{gen}(V)$	$\Delta V_{rad}^{band-tail}(V)$	$\Delta V_{non-rad}$ (V)	$V_{OC}^{mea}(V)$	E_{CT} (eV)	λ (meV)
BHJ	1.530	0.267	0.006	0.056	0.244	0.957	1.405	79
LBL	1.523	0.265	0.006	0.046	0.232	0.975	1.399	70